Article

Investigation of Primary Recrystallization and Decarbonization with Different Heating Rates of Intermediate Annealing Using Nb-Containing Grain-Oriented Silicon Steel

Xin Tian [1], Shuang Kuang [1], Jie Li [2], Jing Guo [2] and Yunli Feng [2,*

[1] Tang Shan Iron & Steel Group Co., Ltd., Tangshan 063016, China; ts_tangsteel@163.com (X.T.); ks_tangs@163.com (S.K.)
[2] College of Metallurgy and Energy, North China University of Science and Technology, Tangshan 063009, China; leijie@ncst.edu.cn (J.L.); gj_hblg@163.com (J.G.)
[*] Correspondence: fengyl@ncst.edu.cn; Tel.: +86-315-8805420

Abstract: An Nb-containing grain-oriented silicon steel was produced through double-stage cold rolling in order to investigate the effect of the heating rate during intermediate annealing on primary recrystallization and decarburization behavior. The microstructure and texture were observed and analyzed by an optical microscope and an electron backscatter diffraction system. A transmission electron microscope was used to observe the precipitation behavior of inhibitors. The decarburization effect during intermediate annealing was also calculated and discussed. The results show that primary recrystallization takes place after intermediate annealing. As the heating rate increases, the average grain size decreases gradually. The textures of {411}<148> and {111}<112> were found to be the strongest along the thickness direction in all of the annealed specimens and are mainly surrounded by HEGB and HAGB (>45°). A large number of inhibitors with the size of 14~20 nm precipitate are distributed evenly in the matrix. The above results indicate that the higher heating rate during intermediate annealing contributes to both an excellent microstructure and magnetic properties. From the calculation, as the heating rate increases, decarbonization tends to proceed in the insulation stage, and the total amount of carbonization declines.

1. Introduction

Grain-oriented silicon steel, which is mainly used as the core material of transformers, is the only product manufactured through a secondary recrystallization process in the steel [1]. The ultimate purpose of its production is to obtain the sharp {110}<001> Goss texture, which possesses the qualities of high magnetic induction and low iron loss, eventually guaranteeing the excellent stability and magnetic properties of finished products [2]. The key technology used to produce grain-oriented silicon steel with the sharp Goss texture is effective control of the inhibitors [3–5]. The most commonly used inhibitors in traditional grain-oriented silicon steel are MnS and AlN [6–8], whose higher solution temperature (>1350 °C) results in a higher slab reheating temperature before hot rolling, inevitably resulting in many bad consequences, such as larger energy consumption, severe equipment damage and higher costs [9]. As such, it is imperative to develop new types of inhibitors to realize slab reheating with a low temperature. The researchers in this study turned their focus to Cu sulfides, which mainly exist in the form of compounds, however, related reports do not express a consistent viewpoint about their specific types and precipitation mechanisms [10–12]. Taking Cu sulfides as the main inhibitor, the slab temperature of grain-oriented silicon steel still needs to be reheated to above 1250 °C [13]. Recently, niobium carbide/nitride is found to have a number of similar features to common inhibitors,

such as the particle size, number and dispersity, and belongs to a kind of stable phase with a slow coarsening rate and low solution temperature, possibly playing a role as the inhibitor in the grain-oriented silicon steel to achieve the goal of slab reheating at a low temperature [14]. Therefore, the element Nb was added into traditional grain-oriented silicon steel and the content of other elements was adjusted accordingly in order to obtain a new type of inhibitor composition on oriented silicon steel with Nb(C,N) as the main inhibitor, and, finally, to realize the slab reheating temperature at under 1250 °C [15,16].

The main inhibitor has changed to Nb-containing grain-oriented silicon, so it is necessary to study the solid solution precipitation behavior of Nb(C,N) in each stage and its influence on the microstructure, texture and magnetic properties. B. Liu et al. analyzed the microstructure and texture of hot rolled Nb-containing grain-oriented silicon steel [17]. F. Fang et al. investigated the effect of Nb on the microstructure, texture and magnetic properties of strip-cast grain-oriented silicon steel [18]. In our previous works, the effect of different slab reheating temperatures was systematically studied, and 1220 °C was found to be the best reheating temperature for Nb-containing grain-oriented silicon steel [16,19].

The decarburizing annealing process in the production of grain-oriented silicon steel is very important for forming good magnetic properties [20]. To date, the reports related to the intermediate annealing of grain-oriented silicon steel are mainly focused on its heating temperature, holding time and annealing atmosphere [21–23], but studies on the heating rate are rarely seen. In general, intermediate annealing is normally used for partial decarburization, while decarburizing annealing after secondary cold rolling is always carried out to ensure that the final carbon content is controlled within 8×10^{-5} [24]. Afterwards, W. Guo et al. found that full decarburizing during intermediate annealing in combination with recovery treatment after the secondary cold rolling can achieve a similar or even better decarbonization effect [25]. The effect of intermediate annealing parameters on the primary recrystallization microstructure, texture and magnetic properties of Nb-containing grain-oriented silicon steel has not been reported, and thus it is not clear whether the same rule is shown with traditional grain-oriented silicon steel. On the basis of Guo's idea, the different heating rates of intermediate annealing were chosen to first study their effects on the microstructure, texture, characteristic grain boundary and inhibitors of primary recrystallization, and then discuss the decarbonization effect, which ultimately helps in determining the best heating rate of Nb-containing grain-oriented silicon steel.

2. Materials and Methods

The material used in this work is the first cold-rolled plate of Nb-containing grain-oriented silicon steel with thickness of 0.75 mm. Its chemical compositions are listed in Table 1. The reduction of the first cold rolling is 70%. Before the first cold rolling, the as-cast billet was first reheated to 1220 °C and held for 20 min in a nitrogen atmosphere, and then hot rolled in six passes to 2.3 mm in thickness with finishing rolling temperature of 870 °C. Subsequently, two-stage normalizing annealing was followed.

Table 1. Chemical compositions of Nb-containing grain-oriented silicon steel (wt.%).

Element	C	Mn	Si	S	Cu	Al	Nb	N	P	Fe
Content	0.041	0.04	3.2	0.0075	0.085	0.023	0.055	0.0085	<0.008	Bal.

The intermediate annealing was conducted in a KBF11Q (Tianjin Zhonghuan Experimental Electric Furnace Co., Ltd., Tianjin, China) rapid thermal annealing furnace under a wet atmosphere of 25% H_2 + 75% N_2, with the water bath temperature of 60 °C. The specimens which were taken from the first cold-rolled plate were first heated to 840 °C at a heating rate of 10 °C/s, 15 °C/s, 20 °C/s, 25 °C/s and 30 °C/s, were then held for 10 min, and subsequently air cooled to room temperature. During the cooling process, H_2 and N_2 were stopped from flowing into the furnace. After intermediate annealing, the annealed plates were cold rolled for a second time, with a rolling reduction of 60%,

and were recovered at 550 °C for 2 min, followed by high temperature annealing at 1200 °C for 8 h, with a heating rate of 50 °C /h and air cooling.

The carbon content of the specimens before and after intermediate annealing with different heating rates was measured by a LECO CS744 (LECO, St. Joseph, MI, USA) high frequency infrared carbon sulfur analyzer. The carbon content of the specimens, which were just heated to the intermediate annealing temperature (840 °C) and then immediately quenched in water, was also measured. Because the decarburization process stops due to a lack of access to gas during the quenching process, the carbon content of the water-quenched specimens was approximately considered as that of when the temperature had just reached 840 °C.

The microstructures of the plate surface and thickness direction of annealed specimens were observed by an Axiovert 200 MAT optical microscope (OM, ZEISS, Tokyo, Japan). The microstructures were characterized with a Zeiss optical microscope and a FEI Quanta FEG 650 field-emission scanning electron microscope (SEM, FEI, Hillsboro, OR, USA), equipped with an electron backscattering diffraction (EBSD, AMETEK, Berwyn, PA, USA) device and TSL OIM Data Collection Software. The grain size analysis, the boundary analysis and the texture analysis of each sample were all calculated from EBSD. The scanning step size was 1.5 μm. The clean-up procedures are as follows: the clean-up type is grain dilation, the grain tolerance angle is 2, and the minimum grain size is 3. The EBSD analysis of each sample is all calculated based on the data of more than 400 grains. The average grain size is calculated using the method of "grain diameter". The {001} pole figures of specimens after high temperature annealing were measured using a Bruker D8 Discover X-ray diffraction and CuKα radiation ($\lambda = 0.15406$ nm, 40 kV, 40 mA) was used for the measurement. Here, the thickness layer was defined by the parameters $S = 2a/d$, where a represented the distance away from the center layer and d was the whole sheet's thickness. $S = 0$, $S = 0.5$ and $S = 1$ represent the surface, subsurface and center layer, respectively.

The observation of inhibitors in the annealed plates was carried out on a JEM-2010 transmission electron microscope (TEM, Nippon Optical Limited, Tokyo, Japan). The specimens for TEM were, first, mechanically ground to 0.05 mm in thickness, and then thinned by a twin-jet electropolishing device at 25 V in a mixture of 5% perchloric acid and 95% ethyl alcohol, with the solution being cooled to about −25 °C with liquid nitrogen. For different heating rates of intermediate annealing, 10 random TEM fields of view with a magnification of 19,500 were chosen to do the quantitative analysis regarding the particle size, number and density. The average particle size was measured by the Image-Pro Plus software. The iron loss $P_{1.7/50}$ (W/kg) and magnetic induction B_{800} (T) of the high temperature annealed plates were measured by a MATS-2010SA (Hunan Lianzhong Technology Co., Ltd., Hunan, China) alternating magnetic measurement device in a single sheet tester, using the permeameter with the size of 30×100 mm^2.

3. Results

3.1. Characteristics of First Cold-Rolled Plate

Figure 1 shows the microstructure, texture and grain boundary characteristics along the thickness direction of the original first cold-rolled plate. In Figure 1a, it can be seen that the first cold-rolled plate, with 70% reduction, is characterized by the banded structure distributed along the rolling direction, and the width of the banded structure is not uniform along the thickness direction. The above phenomenon is attributed to the obvious gradient microstructure which exists in the normalized plate finally being preserved after the first cold rolling [26]. In addition, a certain number of carbides were observed at the grain boundaries, and some shear bands were also found inside the grains. From Figure 1b, the texture types of the surface and subsurface layer for first cold-rolled plate are mainly composed of an α-fiber and γ-fiber texture, with an especially strong intensity of {111}<112> texture transformed from the Goss texture in the normalized plate rotating 35° along two opposite directions [27]. The main texture of the center layer is the rotation cube texture {001}<110> in the α-fiber inherited from the microstructure in the normalized plate due to

its higher stability, which also becomes the main type in the surface and subsurface layer. It is also found that there almost exists no Goss texture along the thickness direction of the first cold-rolled plate. Figure 1c is the grain boundary misorientation distribution of the first cold-rolled plate, in which the green, red and blue line, respectively, represent the low-angle grain boundary (LAGB), with a misorientation angle of <15°; the high energy grain boundary (HEGB), with a misorientation angle of 20°~45°; and the high-angle grain boundary (HAGB), with misorientation angle larger than 45°. Researchers around the world have done a lot of work on the characteristic grain boundary of the grain-oriented silicon steel, and HEGB theory and coincidence site lattice (CSL) theory have gradually become mainstream among the existing theories. HEGB is a kind of HAGB with a misorientation angle of 20°~45° [28,29]. This theory considers HEGB to have the highest energy and migration rate, followed by HAGB with other misorientation angles. In this paper, HAGB is regarded as having a misorientation angle larger than 45°. Both HEGB and HAGB can quickly get rid of the pinning effect of inhibitors, which are beneficial to the abnormal growth of Goss grains during high temperature annealing.
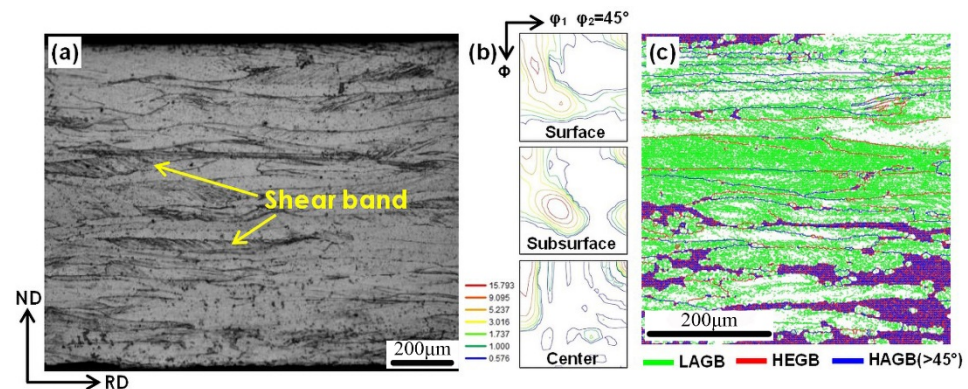

Figure 1. Microstructure (**a**), orientation distribution function (ODFs) at $\varphi^2 = 45°$ section (**b**) and grain boundary misorientation distribution (**c**) along the thickness direction of first cold-rolled plate.

During cold rolling, the equiaxed grains in the normalized plate are pressed into the band structure under the rolling force, but the deformed grains are still surrounded by HAGB. Inside the grain, apart from some HEGB, a great deal of subgrains appear due to the movement of multiple slip systems, which results in a high amount of LAGB existing with high deformation energy. Because of the internal stress of the cold-rolled microstructure, the confidence index of EBSD collected in the area with large internal stress is low and the boundaries of these points with lower confidence indices are marked as HEGB and HAGB as shown in the lower right corner of Figure 1c, which is inaccurate.

3.2. Characteristics of Intermediate Annealed Plate

3.2.1. Effect of Heating Rate of Intermediate Annealing on the Microstructure of Primary Recrystallization

Figure 2 shows the microstructure of the plate surface and thickness directions after intermediate annealing with a heating rate of 30 °C/s, from which it can be seen that the specimen is recrystallized, and the microstructure consists of single ferrite grains. From Figure 2a, the size of the recrystallized grains varies along the surface direction, which is directly related to the energy at the grain boundary of the original cold-rolled plate. The average size of the recrystallized grains, with different heating rates along the surface direction, is measured and listed in Table 2. It is found that the higher heating rate corresponds to relatively small and uniform grains. Gradient microstructure along the thickness direction can be observed, as shown in Figure 2b, with smaller grains in the surface layer and larger ones distributed in the center. During the intermediate annealing process, the carbon content of the surface drops rapidly, and the C atoms continuously diffuse from the center to the plate surface, keeping a high carbon content on the surface

for a long time, which restricts the rapid growth of the nuclei through the pinning effect. From Table 2, it can be seen that as the heating rate increases, the average size of the recrystallized grains along the thickness direction gradually decreases, and the downward trend is the most obvious.
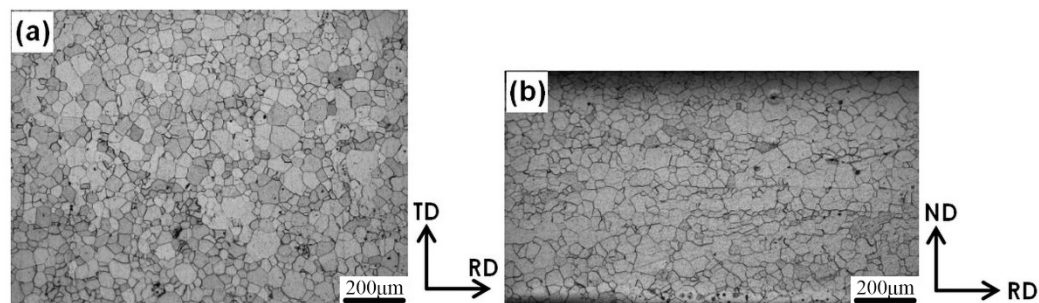

Figure 2. Microstructure of (**a**) plate surface and (**b**) thickness direction after intermediate annealing with heating rate of 30 °C/s.

Table 2. Average grain size of primary recrystallization.

Heating Rate (°C/s)		10	15	20	25	30
Average grain size	Surface	31.25	29.33	28.91	25.1	14.85
(μm)	Thickness	32.44	28.18	27.04	25.38	13.78

The grain morphology along the thickness direction was observed and the grain aspect ratio was obtained from the EBSD results. From Figure 3, it can be seen that with the increase of the heating rate, the grain number with different aspect ratios tends to be even higher, and the aspect ratio of the grains with the largest proportion becomes smaller. The microstructure of the first cold-rolled plate along the thickness direction is known to be the banded structure, and thus the grain aspect ratio is much less than 1, as shown in Figure 1. When the deformed grains are recrystallized, they evolve into equiaxed grains with the aspect ratio being approximate to 1, which is easy to fully grow. However, the grains with larger sizes obtained during primary recrystallization are not beneficial to the abnormal growth of the Goss texture. Therefore, it can be concluded that a certain degree of flatness for the grains after intermediate annealing should be maintained, as this is the most favorable for the subsequent process.

3.2.2. Effect of Heating Rate of Intermediate Annealing on Texture of Primary Recrystallization

Figure 4 shows the orientation distribution functions (ODFs) at $\varphi_2 = 45°$ section of the surface, subsurface and center layers after intermediate annealing with different heating rates. From Figure 4, it can be seen that the texture type for the surface layer of the annealed plate is basically the same at different heating rates, as well as that of the subsurface and center layers, only with certain differences in texture intensity. At the same heating rate, the surface layer has the weakest texture with the type of dominated γ-fiber {111}<112> and {111}<110> texture, weak α-fiber {001}<010> texture and Goss texture {110}<001>. The types of subsurface layer are similar to those of the surface layer composed of strong γ-fiber texture, cube texture {001}<010> and Goss texture, and the overall texture intensity is significantly higher than that at the surface. Compared with the textures in the surface and subsurface layer, the texture type changes in the center layer, with the γ-fiber texture disappearing gradually and the Goss texture becoming obviously weaker than that of the subsurface. Compared with the cold-rolled texture, as seen in Figure 1b, the texture of the annealed specimen distributes more dispersedly and with a lower intensity due to the occurrence of primary recrystallization, however some cold-rolled textures are still retained in the surface and subsurface layers after intermediate annealing.
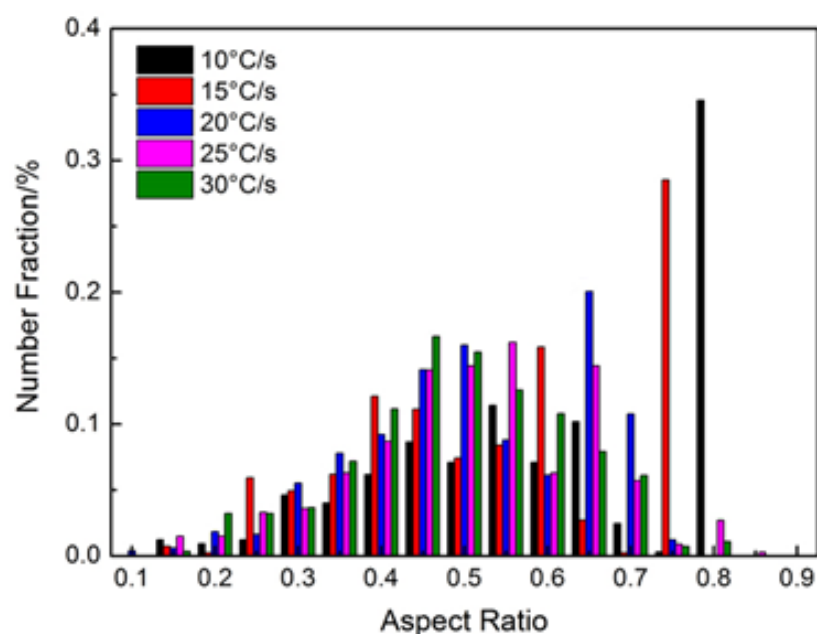
Figure 3. The grain aspect ratio after intermediate annealing with different heating rates along the thickness direction.
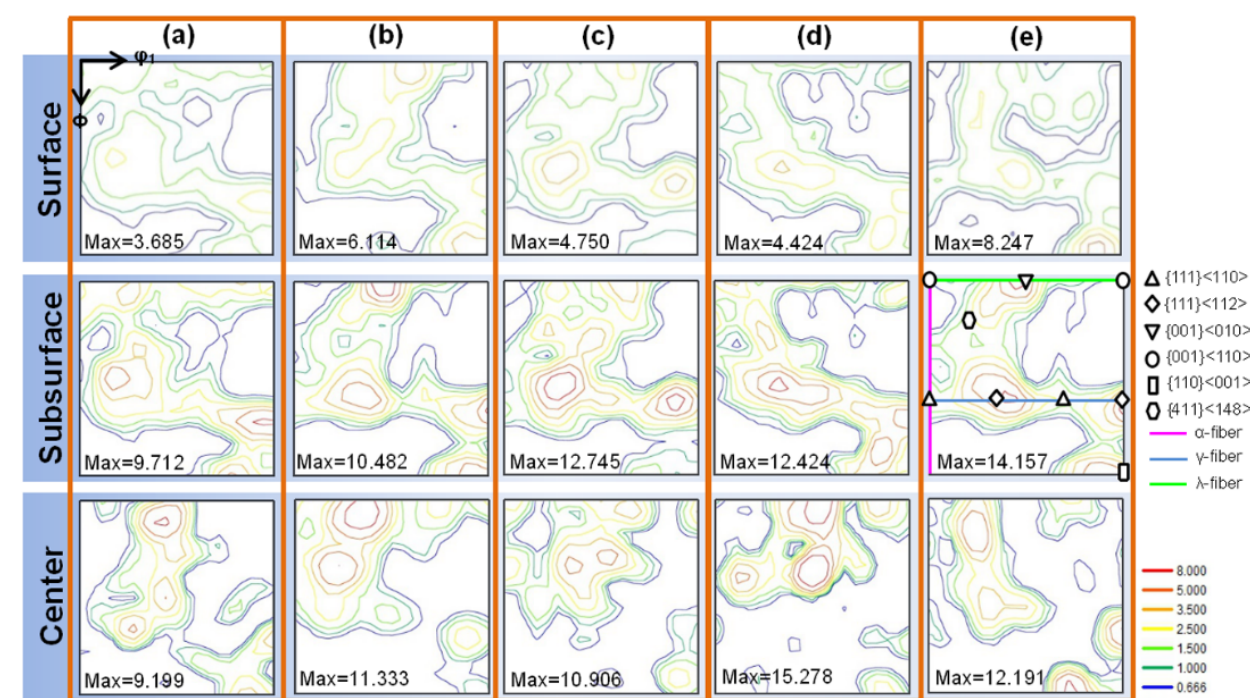

Figure 4. ODFs at $\varphi^2 = 45°$ section of surface, subsurface and center layer along the thickness direction after intermediate annealing with heating rate of (**a**) 10 °C/s, (**b**) 15 °C/s, (**c**) 20 °C/s, (**d**) 25 °C/s and (**e**) 30 °C/s.

Figure 5 illustrates the orientation image maps along the thickness direction of the annealed plates with different heating rates. From Figure 5, it can be seen that the main texture of the annealed plates includes light green {111}<110>, blue {111}<112>, dark green {411}<148> and red Goss {110}<001> textures. The content of the main textures was measured and is listed in Table 3, from which {411}<148> texture is found to be the strongest texture in all of the annealed specimens with different heating rates. When the heating rate is 30 °C/s, the proportion of {411}<148> texture is the highest, at 26.3%, while the lowest reaches up to 21% with a heating rate of 25 °C/s. The content of the textures

in the γ-fiber is also high, especially the {111}<112> texture, which is second only to the {411}<148> texture. When the heating rate is 25 °C/s, the content of the {111}<112> texture is 17.1%, which is comparable with that of the {411}<148> texture of 21%. The Goss texture exists in all of the annealed specimens along the thickness direction, and with the increase of the heating rate, its content also rises.
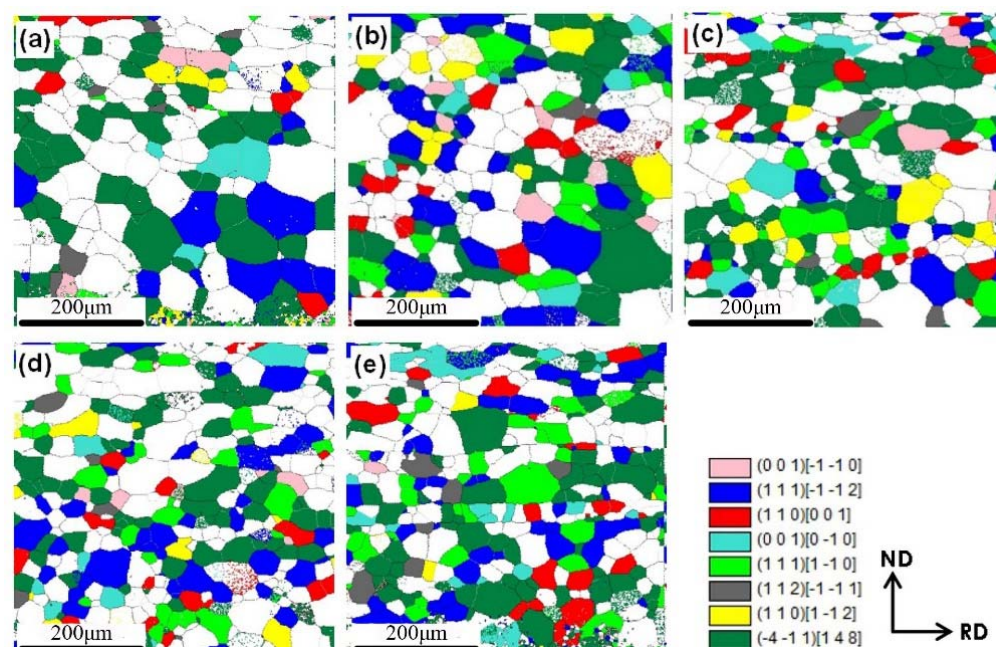

Figure 5. Orientation image maps of several main orientations along the thickness direction after intermediate annealing with heating rates of (**a**) 10 °Cs, (**b**) 15 °C/s, (**c**) 20 °C/s, (**d**) 25 °C/s and (**e**) 30 °C/s.

Table 3. Texture content after intermediate annealing.

Heating Rate (°C/s)	Texture Type (%)			
	{111}<112 >	{111}<110 >	{411}<148 >	{110}<001>
10	10.6	1.4	25.5	2.2
15	14.7	7.1	21.7	3.9
20	11.5	7.5	26.2	5.3
25	17.1	8.5	21.0	5.1
30	13.2	7.4	26.3	6.1

3.2.3. Effect of Heating Rates of Intermediate Annealing on Characteristic Grain Boundary of Primary Recrystallization

Figure 6 shows the grain boundary misorientation distribution along the thickness direction of the annealed plates with a heating rate of 30 °C/s. From Figure 6a, it can be seen that the main textures {110}<001>, {111}<112> and {411}<148> in the annealed plate are mainly surrounded by HEGB and HAGB. From the statistical results regarding the grain boundary, as can be seen in Figure 6b, the proportion of LAGB is the highest with the heating rate of 25 °C/s, while HEGB is at 30 °C/s, and HAGB is at 20 °C/s. When the heating rate is 30 °C/s, the number fractions of HEGB and HAGB are the largest, and the number fraction of LAGB is the least.

CSL theory considers the Σ9 boundaries to have lower energy and higher migration rates than general grain boundaries, and as a result they are less strongly inhibited by Zener drag [30], and then even less so by the Σ5 and Σ3 boundaries. The Σ9 boundaries refers to the boundaries with a misorientation angle of 35° between two adjacent grains, while Σ5 and Σ3 boundaries are 36.9° and 8.5°, respectively. The main CSL boundary is Σ3~Σ11,

and $\Sigma 3$, $\Sigma 5$, $\Sigma 9$ boundaries are focused on in this paper. By analyzing the statistical results in relation to the $\Sigma 3$, $\Sigma 5$, $\Sigma 9$ boundaries after primary recrystallization, one can briefly predict the growing of the Goss grains during high temperature annealing. Figure 7 shows the CSL boundary distribution along the thickness direction of the annealed plates, from which it can be seen that the proportion of $\Sigma 3$ is the highest in the annealed specimens, with a heating rate of 10 °C/s, 15 °C/s, 20 °C/s and 25 °C/s, and then followed by $\Sigma 5$ and $\Sigma 9$. When the heating rate is 30 °C/s, the proportion of $\Sigma 9$ is the highest, and is much higher than that of other heating rates.
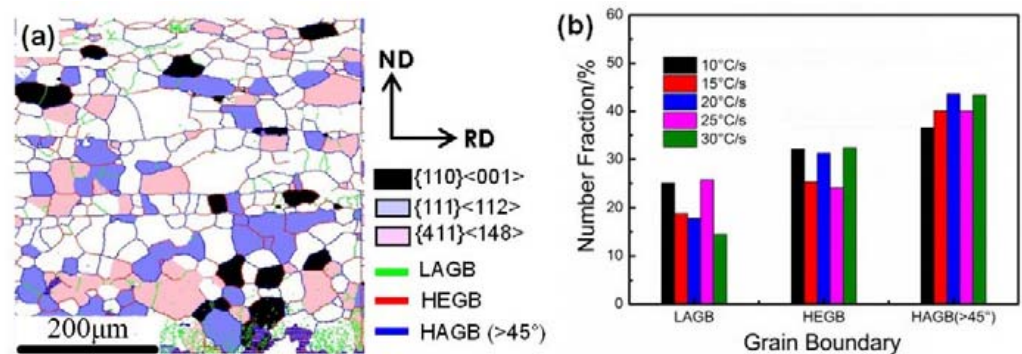

Figure 6. Grain boundary misorientation distribution after intermediate annealing with heating rate of 30 °C/s (**a**) and LAGB, HEGB and HAGB (>45°) fractions with different heating rates of intermediate annealing (**b**).
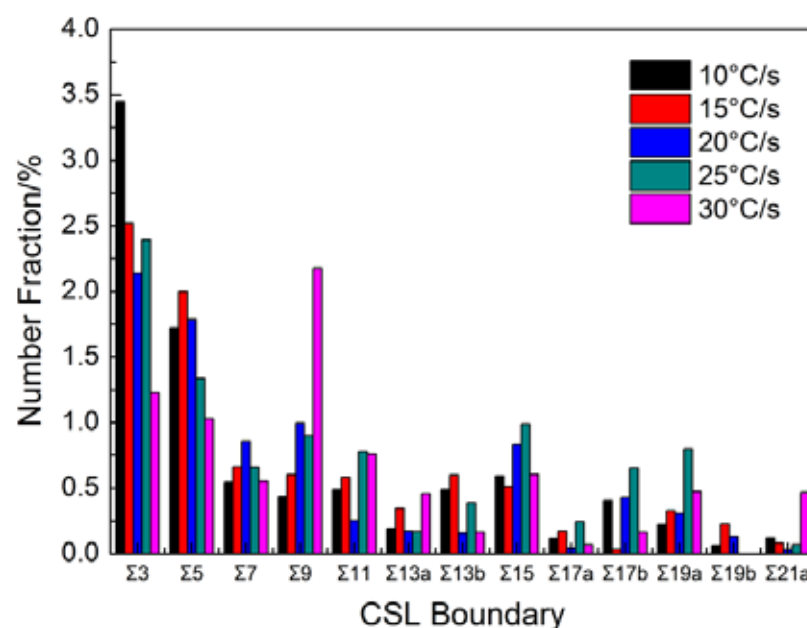

Figure 7. CSL boundary distribution after intermediate annealing with different heating rates.

3.2.4. Effect of Heating Rate of Intermediate Annealing on Inhibitors of Primary Recrystallization

In the Nb-containing grain-oriented silicon steel, the main inhibitor is Nb(C,N) with a lower precipitation temperature, and the assistant one contains MnS, AlN, Cu sulfides, whose combination can realize the slab reheating with a low temperature [16]. Figure 8 shows the TEM morphology of inhibitors and the statistical results of the mean size and volume fraction of the inhibitors. In addition to the common inhibitors AlN and MnS that occur in traditional grain-oriented silicon steel, Nb(C,N) is also formed due to the addition

of Nb in the steel, as shown in Figure 8g–i. The morphology of Nb(C,N) and MnS is mainly spherical or ellipsoid, while the morphology of AlN is mainly square.
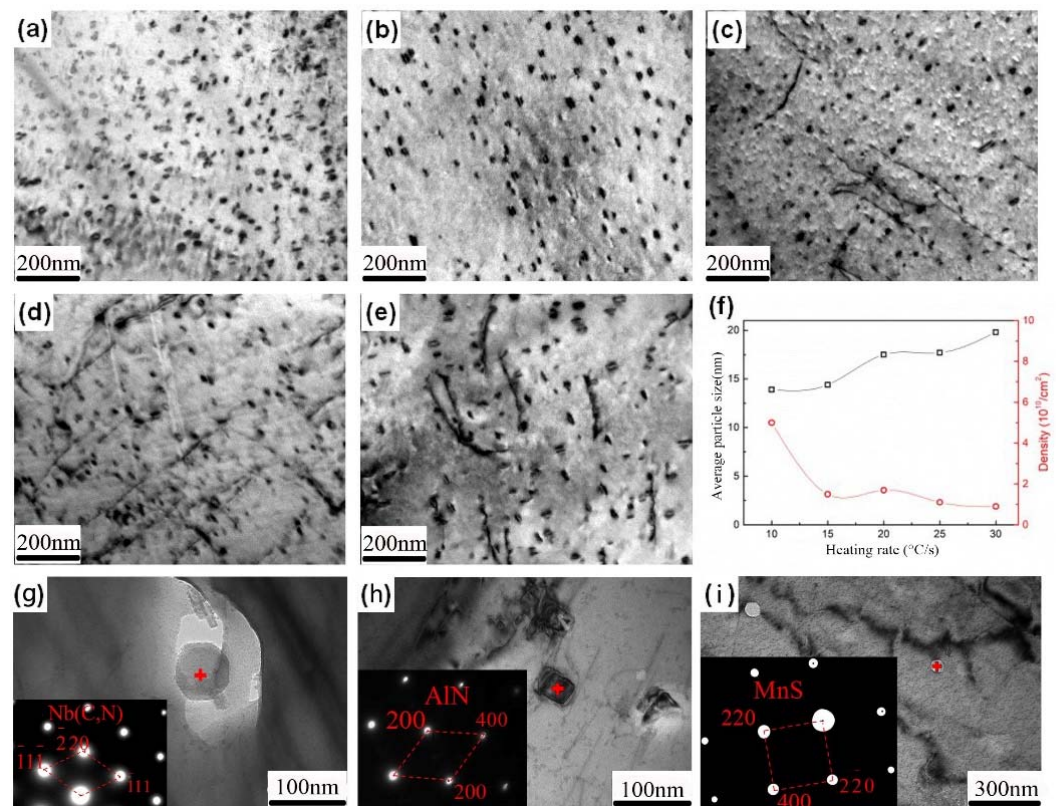

Figure 8. TEM morphology of the inhibitors after intermediate annealing with heating rate of (**a**) 10 °C/s, (**b**) 15 °C/s, (**c**) 20 °C/s, (**d**) 25 °C/s and (**e**) 30 °C/s, and (**f**) statistical results of the mean size and volume fraction of the inhibitors, the electron diffraction patterns of inhibitors (**g**) Nb(C,N), (**h**) AlN and (**i**) MnS.

From Figure 8a–e, after intermediate annealing, a large number of inhibitors with small size precipitates disperse and distribute evenly in the matrix. Furthermore, it is also found that with higher heating rates, there still exists a certain dislocation line in the matrix (see Figure 8c–e, on which some inhibitors are also observed to precipitate due to the higher energy). From Figure 8f, it can be seen that the average size of the inhibitors is located in the range of 14~20 nm, which meets the size requirement of the inhibitors playing the inhibiting effect. As the heating rate increases, the average diameter of the inhibitors shows a slow rising trend in general, but the volume fraction is in decline. It is only the presence of these inhibitors that can prevent the normal growth of the first recrystallized grains, shown in Figure 2, and ensure the smooth subsequent secondary recrystallization.

3.3. Decarbonization Effect during Intermediate Annealing

In the grain-oriented silicon steel, there is always a certain amount of carbon in the matrix, which has two main functions. One function is to enlarge the γ phase area, refining the microstructure during hot rolling. On the other hand, the austenite-containing element C can prevent the abnormal growth of secondary recrystallized ferrite during high temperature annealing, leaving some other oriented grains in the plate and finally reducing the magnetic properties of the finished products. Therefore, it is very important to decarbonize completely during intermediate annealing.

During intermediate annealing, the furnace is filled with H_2 and N_2. A weak oxidative atmosphere is formed in the furnace by heating water vapor with H_2 and N_2. In the

grain-oriented silicon steel, decarbonization is accomplished through the reaction between C in the matrix and water vapor. The reaction equation is as follows:

$$C + H_2O = CO + H_2 \tag{1}$$

H_2 and N_2 are allowed to pass through the furnace during the heating and insulation stage only, and are stopped from doing so during cooling process, when the decarbonization also ends. As such, decarbonization mainly occurs in the heating and insulation stage of the intermediate annealing.

Table 4 lists the decarbonization amount in the heating stage. It can be seen that as the heating rate increases, the decarbonization amount decreases gradually. Further studies also found that the decarburization amount is approximately inversely proportional to the heating rate. The expression is as follows:

$$v = f / \Delta C \tag{2}$$

where v the heating rate, ΔC is decarbonization amount in the heating stage, and f is the constant.

Table 4. Original carbon content C_0 before the intermediate annealing, carbon content when reaching the intermediate annealing temperature of 840 °C $C_{840\,°C}$ and decarburization amount ΔC in heating stage. f is constant in Equation (2).

Heating Rate (°C/s)	C_0 (%)	$C_{840\,°C}$ (%)	ΔC (%)	f
10	0.040	0.021	0.019	0.190
15	0.040	0.027	0.013	0.195
20	0.040	0.030	0.010	0.200
25	0.040	0.032	0.008	0.200
30	0.040	0.033	0.007	0.210

From Equation (1), the f value, corresponding to different heating rates, can be obtained. As shown in Table 4, five groups of f values fluctuate around 0.20.

In the insulation stage of intermediate annealing, the initial carbon content is considered to be the final carbon content in the heating stage, i.e., $C_{840°C}$ in Table 4. During the actual decarburization process, the reaction rate is mainly controlled by two parameters. One is the coverage of oxygen on the surface of the plate, namely the degree of oxidation θ_0, which is determined by temperature function and partial pressure ratio between water vapor and H_2 in the mixed atmosphere. θ_0 can be expressed by:

$$\theta_0 = \frac{K_0 P_{H_2O} / P_{H_2}}{1 + K_0 P_{H_2O} / P_{H_2}} \tag{3}$$

where K_0 is the temperature function, and P_{H_2O} / P_{H_2} is the partial pressure ratio between water vapor and H_2.

Considering the volume fraction and flow of H_2 and N_2, as well as some constants, such as water bath temperature, humidity, dew point temperature and the saturated vapor pressure, the partial pressure ratio between water vapor and H_2 is deduced as 1.176.

The other parameter that affects the reaction rate of decarburization is the kinetic constant of the surface decarburization reaction rate k (cm/s):

$$k = 5,611,000 \exp(-197,000 / RT) \tag{4}$$

According to Fick's first law, the carbon flux J_c ($x = 0, t$) (cm/s) in the gas-solid reaction interface of Nb-containing grain-oriented silicon steel can be obtained:

$$J_c(x = 0, t) = -D\frac{dC}{dx} = k \times \theta_0 \times C(x = 0, t) \tag{5}$$

where D is the diffusion coefficient of carbon in ferrite, $D = 2.2\exp(-123,000/RT)$.

The carbon diffusion inside the Nb-containing grain-oriented silicon steel is consistent with Fick's second law:

$$\frac{dC}{dt} = D\frac{d^2C}{dx^2} \tag{6}$$

The decarbonization kinetics of Nb-containing grain-oriented silicon steel were calculated and analyzed using a finite-difference iterative method according to the above equations, and the carbon content at different times is listed in Table 5. From Table 5, it can be seen that as the decarbonization time prolongs, the carbon content first decreases rapidly, and then gradually slows down. After 10 min of decarbonization, the carbon content is basically unchanged, which meets the standard for industrial production. If the decarbonization time continues to extend, it would be no good for decarbonization, and the production cost would also increase. Meanwhile, insulation for a long time leads to grain growth, which is not beneficial for secondary recrystallization. Comparing the decarbonization amounts at different stages from Tables 4 and 5, it can be found that as the heating rate increases, decarbonization tends to proceed in the insulation stage, and the total amount ($\Delta C + \Delta C'$) declines. In addition, from the calculated and measured decarbonization amount, the deviation exists within the tolerance range, which indicates the applicability of the selected equations and the accuracy of the calculation.

Table 5. Calculated and experimental carbon content and decarburization amount $\Delta C'$ in the insulation stage of intermediate annealing.

Heating Rate (°C/s)	Calculated Results (%)						Experimental Results (%)	$\Delta C'$ (%)
	0 s ($C_{840\,°C}$)	120 s	240 s	360 s	480 s	600 s	600 s	
10	0.021	0.013	0.008	0.005	0.004	0.003	0.002	0.019
15	0.027	0.014	0.010	0.006	0.005	0.004	0.003	0.024
20	0.030	0.017	0.013	0.010	0.008	0.006	0.005	0.025
25	0.032	0.020	0.014	0.010	0.008	0.006	0.006	0.026
30	0.033	0.025	0.018	0.012	0.009	0.007	0.007	0.026

3.4. Characteristics of High-Temperature Annealed Plates

The specimens with different heating rates of intermediate annealing after high temperature annealing are all characterized and the characteristics of specimens with 30 °C/s are shown in Figure 9. From Figure 9a, it can be seen that secondary recrystallization occurs after high temperature annealing, with coarse recrystallized grains distributing on the plate surface on the centimeter scale, but with some grains being small in size, indicating that they did not grow up completely. From the pole figure in Figure 9b, it can be seen that the grains on the plate surface are mainly Goss texture. Apart from this, there are still some grains with other orientations, such as {411}<148> texture in Figure 9c, which were not totally swallowed by the Goss grains. Furthermore, inhibitors also change significantly after high temperature annealing compared to those in Figure 8. From Figure 9d, it can be seen that the density of the inhibitors reduces greatly, and most of them dissolve into the matrix, which enable the Goss grains to break the pinning effect and achieve abnormal grain growth. However, some undissolved inhibitors can also be found with a size larger than 100 nm, which shows that the inhibitors happen to coarsen and fail to cause a pinning effect, finally being preserved in the plate. After high temperature annealing, the magnetic properties of specimens with different heating rates were measured and are shown in

Table 6. It can be seen that when the heating rate is 30 °C/s, the magnetic properties are the best, with the magnetic induction of 1.88 T and iron loss of 1.34 W/kg.
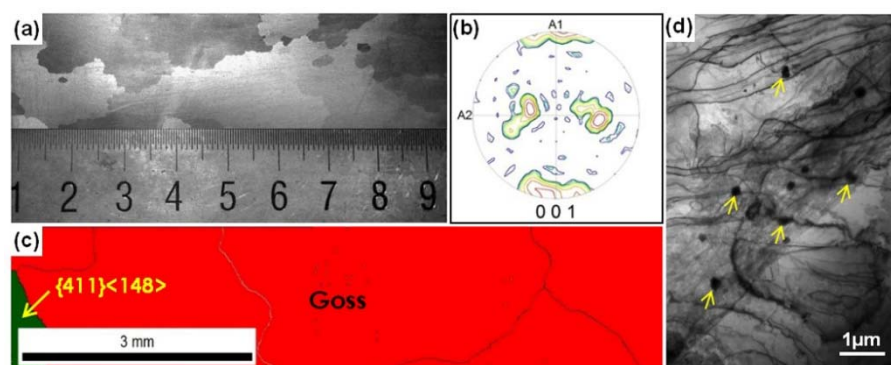

Figure 9. Macrostructure (**a**), {001} pole figure (**b**), EBSD orientation image map (**c**) and TEM morphology (**d**) after high temperature annealing with heating rate of 30 °C/s.

Table 6. Magnetic induction B_{800} and iron loss $P_{1.7/50}$ after intermediate annealing.

Heating Rate (°C/s)	B_{800} (T)	$P_{1.7/30}$ (W/kg)
10	1.63	1.42
15	1.80	1.39
20	1.72	1.36
25	1.83	1.37
30	1.88	1.34

4. Discussion

In order to investigate the effect of different heating rates during the intermediate annealing process, the recrystallized microstructure, texture, grain boundary characteristics and inhibitors are discussed below.

As the heating rate increases, the average grain size along the plate surface and thickness direction tends to decrease and is less than 15 μm, especially when the heating rate is 30 °C/s. In addition, when the heating rate is within 10~25 °C/s, the differences in the grain sizes do not exceed 5 μm with every 5 °C/s rate. However, when the heating rate increases from 25 °C/s to 30 °C/s, the differences in the grain size are all larger than 10 μm (see Table 2). This shows that the obtained grains are extremely small after intermediate annealing, with a heating rate of 30 °C/s. Moreover, with the increase of the heating rate, the aspect ratio shows a declining trend, which can effectively prevent recrystallized grains growing oversized and contribute to the abnormal growth of Goss grains during high temperature annealing.

From the point of view of obtaining high magnetism of grain-oriented silicon steel, generally, the best texture distribution after primary recrystallization is strong γ-fiber texture and Goss texture distributing in the surface and subsurface, as well as some Goss grains being preserved at the center [31]. Among the recrystallized grains in Nb-containing grain-oriented silicon steel, HEGBs are formed between Goss grains and γ-fiber {111}<112>/{411}<148> grains. It has been reported that the orientation between {111}<112> and Goss grains are close to Σ9 relationship, and {411}<148> grains are related to Goss grains by Σ9 orientation relationship (rotate along RD axis) [32]. Therefore, both {111}<112> and {411}<148> grains are beneficial to the secondary recrystallization of Goss grains, thus contributing to the useful texture. When the heating rate is 30 °C/s, γ-fiber and Goss textures in the surface and subsurface layer have a higher intensity compared with other heating rates, and {111}<112> orientation is relatively more accurate. In contrast, the γ-fiber texture has undergone a marked deflection with a heating rate of 10 °C/s and 15 °C/s (see Figure 4). Meanwhile, the intensity of the {411}<148> texture at 30 °C/s nearly reaches the

largest value in the surface, subsurface and center layers. It is also found that the {111}<112> texture has the highest content at 25 °C/s, but both the content of {411}<148> texture and total content of the useful textures {111}<112> and {411}<148> are the highest at 30 °C/s (see Table 3), which demonstrate that the obtained texture after primary recrystallization with a higher heating rate is the most favorable for the growth of Goss grains.

In consideration of characteristic grain boundary, the total content of HEGB and HAGB is the highest, while LAGB is the lowest after intermediate annealing with a heating rate of 30 °C/s (see Figure 6). Additionally, the content of Σ9 boundaries reaches the maximum value at 30 °C/s and is much higher than those of other heating rates, followed by Σ3 and Σ5 boundaries (see Figure 7). The above results show that the overall migration speed of the grain boundary is the fastest with a heating rate of 30 °C/s.

Generally, the inhibitors first dissolve into the matrix during the heating and insulation stage of the intermediate annealing, and then precipitate from the matrix during the cooling process. If the heating rate is fast, which means that the time for the heating process shortens accordingly, the inhibitors are not able to dissolve into the matrix completely, resulting in the amount of precipitation dropping inevitably during the subsequent cooling process. In addition, some inhibitors precipitate and center on the undissolved particles, forming the composite precipitations with a larger size. Finally, the number of the obtained inhibitors is relatively low and the size is relatively large (see Figure 8). However, the results from using the faster heating rate show the better characteristics of primary recrystallization and the magnetic properties of the final product, which indicate that the inhibitors formed during primary recrystallization do not just require a large quantity and small size. Therefore, how to control the precipitation of inhibitors and maximize their role needs further investigation.

In conclusion, the specimen annealed with higher heating rate possesses the best primary recrystallized microstructure and texture, which guarantees the abnormal growth of Goss texture after high temperature annealing and results in the best magnetic properties.

5. Conclusions

(1) First recrystallization occurs after intermediate annealing. The size of the recrystallized grains varies along the surface direction, and the gradient microstructure presents along the thickness direction. Both the surface and subsurface layers are composed of strong γ-fiber texture after intermediate annealing, while the Goss texture becomes weaker in the center. The {411}<148> and {111}<112> textures are found to be the strongest along the thickness direction in all of the annealed specimens with different heating rates.

(2) The useful texture {111}<112> and {411}<148 >, as well as the Goss texture in the annealed plate, are mainly surrounded by HEGB and HAGB (>45°). When the heating rate is 30 °C/s, the proportion of Σ9 is the highest, the total content of HEGB and HAGB is the largest, and the content of LAGB is the least.

(3) A large number of inhibitors with a size of 14~20 nm precipitate disperse and distribute evenly in the matrix after intermediate annealing. As the heating rate increases, the average diameter of inhibitors shows a slow rising trend in general, but the volume of the fraction is in decline.

(4) The decarburization amount is approximately inversely proportional to the heating rate in the heating stage of the intermediate annealing process. In the insulation stage, as the decarbonization time prolongs, the carbon content first decreases rapidly, and then gradually slows down. As the heating rate increases, decarbonization tends to proceed in the insulation stage, and the total amount declines.

Institutional Review Board Statement: Not applicable.

Informed Consent Statement: Not applicable.

Data Availability Statement: No new data were created or analyzed in this study. Data sharing is not applicable to this article.

Conflicts of Interest: The authors declare no conflict of interest.

References

1. Harase, J.; Shimizu, R.; Dingley, D.J. Texture evolution in the presence of precipitates in Fe-3%Si alloy. *Acta Mater.* **1991**, *39*, 763–770. [CrossRef]
2. Hayakawa, Y.; Kurosawa, M. Orientation relationship between primary and secondary recrystallized texture in electrical steel. *Acta Mater.* **2002**, *50*, 4527–4534. [CrossRef]
3. Fang, F.; Zhang, Y.-X.; Lu, X.; Wang, Y.; Cao, G.-M.; Yuan, G. Inhibitor induced secondary recrystallization in thin-gauge grain oriented silicon steel with high permeability. *Mater. Des.* **2016**, *105*, 398–403. [CrossRef]
4. Nam, S.K.; Kim, G.H.; Lee, D.N.; Kim, I. New process for the Goss texture formation and magnetic property in silicon steel sheet by hot asymmetric rolling and annealing. *Metall. Mater. Trans. A* **2018**, *49*, 1841–1850. [CrossRef]
5. Wang, Y.; Xu, Y.-B.; Zhang, Y.-X.; Xie, S.-Q.; Yu, Y.-M.; Wang, G.-D. On abnormal growth of {210}<001> grain in grain-oriented silicon steel. *Mater. Res. Bull.* **2015**, *69*, 138–141. [CrossRef]
6. Kustas, A.B.; Sagapuram, D.; Trumble, K.P.; Chandrasekar, S. Texture development in high-silicon iron sheet produced by simple shear deformation. *Metall. Mater. Trans. A* **2016**, *47*, 3095–3108. [CrossRef]
7. Li, H.; Feng, Y.-L.; Song, M.; Liang, J.-L.; Cang, D.-Q. Effect of normalizing cooling process on microstructure and precipitates in low-temperature silicon steel. *Trans. Nonferrous Met. Soc. China* **2014**, *24*, 770–776. [CrossRef]
8. Salih, M.Z.; Weidenfeller, B.; Al-hamdany, N.; Brokmeier, H.-G.; Gan, W.M. Magnetic properties and crystallographic textures of Fe 2.6% Si after 90% cold rolling plus different annealing. *J. Magn. Magn. Mater.* **2014**, *354*, 105–111. [CrossRef]
9. Matsuo, M. Texture control in the production of grain oriented silicon steels. *ISIJ Int.* **1989**, *29*, 809–827. [CrossRef]
10. Jenkins, K.; Lindenmo, M. Precipitates in electrical steels. *J. Magn. Magn. Mater.* **2008**, *320*, 2423–2429. [CrossRef]
11. Ueshima, N.; Maeda, T.; Oikawa, K. Effect of Cu addition on precipitation and growth behavior of MnS in silicon steel sheets. *Metall. Mater. Trans. A* **2017**, *48*, 3843–3851. [CrossRef]
12. Cui, F.-E.; Yang, P.; Mao, W.-M. Behaviors of different inhibitors during secondary recrystallization of a grain-orientated silicon steel. *Int. J. Min. Met. Mater.* **2011**, *18*, 314–319. [CrossRef]
13. Wu, Y.; Li, F.-J.; Wang, T.; Zhao, D.; Huang, H.-F.; Li, H.-G.; Zheng, S.-B. Influence of Cu_2S precipitates dissolution on ferrite grain growth during heat treatment in the non-oriented electrical steel sheet. *Met. Mater. Int.* **2017**, *23*, 618–624. [CrossRef]
14. Bian, X.-H.; Zeng, Y.-P.; Nan, D.; Wu, M. The effect of copper precipitates on the recrystallization textures and magnetic properties of non-oriented electrical steels. *J. Alloys Compd.* **2014**, *588*, 108–113. [CrossRef]
15. Li, H.; Feng, Y.-L.; Zhang, D.; Song, M.; Cang, D.-Q. Balanced solubility product and enthalpies of formation of Nb compounds in 0.09% oriented silicon steel. *Rare Met.* **2013**, *32*, 318–322. [CrossRef]
16. Feng, Y.-L.; Guo, J.; Li, J.; Ning, J.-L. Effect of Nb on solution and precipitation of inhibitors in grain-oriented silicon steel. *J. Magn. Magn. Mater.* **2017**, *426*, 89–94. [CrossRef]
17. Liu, B.; Song, X.-L.; Zhu, R.-Q.; Jia, J. Analysis of textures and precipitates of hot rolled Nb-bearing low temperature oriented silicon steel strip. *J. Iron Steel Res.* **2017**, *10*, 823–830.
18. Fang, F.; Lan, M.-F.; Lu, X.; Zhang, Y.-X.; Wang, Y.; Yuan, G.; Cao, G.-M.; Xu, Y.-B.; Misra, R.D.K.; Wang, G.-D. The impact of niobium on the microstructure, texture and magnetic properties of strip-cast grain oriented silicon steel. *J. Magn. Magn. Mater.* **2017**, *442*, 1–7. [CrossRef]
19. Feng, Y.-L.; Li, Y.; Guo, J.; Li, J.; Du, T.-T. Effect of slab reheating temperature on recrystallization microstructure, texture and magnetic properties of Nb-containing grain- oriented silicon steel. *J. Magn. Magn. Mater.* **2017**, *439*, 135–143. [CrossRef]
20. Song, H.-Y.; Liu, H.-T.; Liu, W.-Q.; Wang, Y.-P.; Liu, Z.-Y.; Wang, G.-D. Effects of two-stage cold rolling schedule on microstructure and texture evolution of strip casting grain-oriented silicon steel with extra-low carbon. *Metall. Mater. Trans. A* **2016**, *47*, 1770–1781. [CrossRef]
21. Vorob'ev, G.M.; Popova, V.I. Texture of deformation and secondary recrystallization of silicon iron after intermediate annealing. *Met. Sci. Heat Treat.* **1969**, *11*, 889–891. [CrossRef]

22. Salih, M.Z.; Weidenfeller, B.; Al-hamdany, N.; Brokmeier, H.-G.; Gan, W.M. The effect of intermediate annealing between cold rolled steps on crystallographic texture and magnetic properties of Fe–2.6% Si. *J. Magn. Magn. Mater.* **2014**, *362*, 141–149. [CrossRef]

23. Lobanov, M.L.; Gomzikov, A.I.; Akulov, S.V.; Pyatygin, A.I. Decarburizing annealing of technical alloy Fe-3% Si. *Met. Sci. Heat Treat.* **2005**, *47*, 478–483. [CrossRef]

24. He, Z.-Z.; Zhao, Y.; Luo, H.-W. *Electrical Steel*; Metallurgical Industry Press: Beijing, China, 2012; pp. 422–424. (In Chinese)

25. Guo, W.; Mao, W.-M.; Li, Y.; An, Z.-G. Influence of intermediate annealing on final Goss texture formation in low temperature reheated Fe-3%Si steel. *Mater. Sci. Eng. A* **2011**, *528*, 931–934. [CrossRef]

26. Ling, C.; Xiang, L.; Qiu, S.-T.; Gan, Y. Effects of normalizing annealing on grain-oriented silicon steel. *J. Iron Steel Res. Int.* **2014**, *21*, 690–694. [CrossRef]

27. Tomida, T.; Tanaka, T. Development of (100) texture in silicon steel sheets by removal of manganese and decarburization. *ISIJ Int.* **1995**, *35*, 548–556. [CrossRef]

28. Hayakawa, Y.; Szpunar, J.A. The role of grain boundary character distribution in secondary recrystallization of electrical steels. *Acta Mater.* **1997**, *45*, 1285–1295. [CrossRef]

29. Hayakawa, Y.; Szpunar, J.A. A new model of Goss texture development during secondary recrystallization of electrical steel. *Acta Mater.* **1997**, *45*, 4713–4720. [CrossRef]

30. Homma, H.; Hutchinson, B. Orientation dependence of secondary recrystallisation in silicon–iron. *Acta Mater.* **2003**, *51*, 3795–3805. [CrossRef]

31. Chang, S.-K. Texture change from primary to secondary recrystallization by hot-band normalizing in grain-oriented silicon steels. *Mater. Sci. Eng. A* **2007**, *452*, 93–98. [CrossRef]

32. Kim, J.K.; Lee, D.N.; Koo, Y.M. The evolution of the Goss and Cube textures in electrical steel. *Mater. Lett.* **2014**, *122*, 110–113. [CrossRef]